Investigation of single-walled carbon nanotubes with a low-energy electron point projection microscope

2013 New J. Phys. 15 043015

(http://iopscience.iop.org/1367-2630/15/4/043015)

New Journal of Physics
The open access journal for physics

Investigation of single-walled carbon nanotubes with a low-energy electron point projection microscope

Ing-Shouh Hwang[1,5], Che-Cheng Chang[1], Chien-Hung Lu[1,4], Shih-Chin Liu[1], Yuan-Chih Chang[1], Ting-Kuo Lee[1], Horng-Tay Jeng[1,3], Hong-Shi Kuo[1], Chun-Yueh Lin[1,2], Chia-Seng Chang[1] and Tien T Tsong[1]

[1] Institute of Physics, Academia Sinica, Nankang, Taipei, Taiwan, Republic of China
[2] Department of Physics, National Taiwan University, Taipei, Taiwan, Republic of China
[3] Department of Physics, National Tsing Hua University, Hsinchu 300, Taiwan, Republic of China
E-mail: ishwang@phys.sinica.edu.tw

New Journal of Physics **15** (2013) 043015 (14pp)
Received 21 December 2012
Published 11 April 2013
Online at http://www.njp.org/
doi:10.1088/1367-2630/15/4/043015

Abstract. There has been controversy about the interpretation of the interference patterns recorded with low-energy electron point projection microscopy. With a highly coherent single-atom electron source, we have used a point projection microscope (PPM) to image a suspended and isolated single-walled carbon nanotube at different tip–sample separations. The nanotube and the surrounding structure are also imaged with a transmission electron microscope. Through numerical simulations, we can fit well the interference patterns of the nanotube recorded by the PPM at different separations. Our simulation results indicate that the interference patterns can be considered as electron holograms at large tip–sample separations (or small magnifications). However, at small tip–sample separations, the interference patterns are dominated by the biprism effect due to significant charge density induced

[4] Current address: Department of Electrical Engineering, Princeton University, Princeton, NJ 08544, USA.
[5] Author to whom any correspondence should be addressed.

on the nanotube, and thus, the interference patterns contain little information about the internal structure of the object. The results provide a reason why the images obtained by point projection microscopy so far have never achieved a resolution smaller than 2 nm. New research directions for achieving high-resolution imaging of biological molecules with low-energy electrons are also discussed.

Contents

1. Introduction

Imaging of nano-objects with low-energy electrons offers significant advantages over the use of high-energy electrons. Firstly, the radiation damage is very low, especially for imaging bio-organic molecules. Secondly, the scattering cross sections of atoms for low-energy electrons are high, and thus, high contrast for light atoms, such as carbon, can be obtained. In 1989, Stocker, Fink and co-workers developed an electron microscope based on projection of a low-energy electron point source (LEEPS) and successfully imaged carbon fibers of 10–20 nm [1, 2]. When the magnification was high enough, interference fringes could be seen to be superposed on the shadow image of the object. The microscopy was called 'holography with low-energy electrons' and it was suggested that atomic resolution of the object might be achieved through reconstruction from the obtained electron holograms [3, 4]. Since then, a number of research groups have built similar electron microscopes and imaged various nano-objects [5–17]. There are several names for this type of microscope, including the low-energy electron point source microscope, the Fresnel projection microscope, or the low-energy electron point projection microscope (low-energy electron PPM, or PPM for short), etc. From the numerous works over the last two decades, however, there has been controversy about whether the interference patterns can be considered as electron holograms. In addition, the best resolution achieved so far by this type of low-energy electron microscopy is about 2 nm [18]. It would be important to understand whether there is a resolution limit for this technique and what physical effect causes the limitation. Gaining an understanding of the mechanism can help in the development of better coherent electron imaging techniques, including electron in-line holography and coherent electron diffraction microscopy.

Gabor [19] proposed the concept of holography in 1948. In this scheme, an electron beam of sufficient coherence is focused on a very small spot to illuminate a thin object placed at a short distance behind the focus point. A screen placed behind the object records the amplitude distribution. It is assumed that most of the electron beam passes through the object without interaction and forms the reference wave. Only a small portion of the electron wave is elastically

scattered at the object and gives rise to a phase shift in comparison with the reference wave. The constructive and destructive interference between the reference wave and the elastically scattered wave produces a hologram on the screen. This projection method was later called 'in-line holography'.

The LEEPS microscope developed by Fink *et al* [1, 2] is basically a point projection microscope (PPM) demonstrated by Morton and Ramberg in 1939 [20]. The PPM is a shadow microscope where an object is placed between a field emission electron point source and a screen. The shadow image of the object can be seen on the screen with a magnification equal to the ratio of the source–screen separation to the source–object separation. Images obtained with this type of microscopy are free from spherical aberrations because no lens elements are involved. The major improvements made by Fink *et al* [1, 2] were that they used a highly coherent electron point source and that the tip–object separation could be well controlled to a very small distance. They had considered this microscope a physical realization of the in-line holography proposed by Gabor and thus used 'holograms' to name the interference patterns recorded in the PPM images [2]. Typical electron energies used in the PPM are 20–500 eV, much smaller than those in modern high-voltage electron microscopes. Using a PPM, Germann *et al* [21] recently demonstrated that DNA could withstand a high dose of coherent low-energy electron radiation with little damage. The study suggested that there was hope for reconstructing the atomic structure of biomolecules using holographic imaging of PPM.

Binh *et al* [5] also developed a similar PPM using atomic-size electron sources and observed similar interference patterns to that reported by Fink *et al.* However, they thought that the patterns could be well explained by Fresnel diffraction and were not holograms as had been asserted by Fink *et al.* Later, Prigent and Morin [10] simulated the interference patterns of carbon fibers observed in their PPM images by assuming a positive charge density on isolated fibers. In their modeling, the fibers were assumed to be opaque to the low-energy electron beam. From their simulations, a positively charged fiber acts as a small convergent electron biprism and the fringe pattern depends strongly on the charge density of the fibers. Through ray tracing calculations, Weierstall *et al* [9] also showed that a fiber stretched across a hole played the role of a biprism in a PPM, because the potential around the fiber bends with the voltage applied between the tip and the fiber. Later, Cho *et al* [14] also demonstrated that multiwalled carbon nanotubes (MWNTs) worked as a nanobiprism in their PPM experiments. Using the MWNTs, they could measure the spatial coherence of the electron beam from their field emitters.

An important question has arisen: namely, the question of whether the interference patterns seen in PPM images can be viewed as the holograms proposed by Gabor. The object considered by Gabor should be thin enough to be transparent to the electron beam. It is known that the inelastic mean free path for low-energy electrons of 20–500 eV is 0.5–1.0 nm [22], which is equivalent to the thickness of two to three graphene layers. Most one-dimensional (1D) nano-objects imaged by PPM so far, including the carbon fibers and DNA molecules, are much too thick to be transparent for the low-energy electron beams. Thus the interference patterns reported in early PPM works might not result from the 'phase shift' of the elastically scattered wave passing through the objects. Therefore, it would be desirable to use PPM to image a very thin object that is transparent to the low-energy electrons. By making a comparison with theoretical simulations, we can determine the relative contributions from the holographic effect and the biprism effect. This would not only improve the interpretation of the PPM images but also help in theoretical reconstruction of the object structure from PPM images.

We note that there is a major difference in the electron sources proposed by Gabor and by Fink *et al.* Gabor proposed to focus an electron beam to a fine point, which is used as a coherent point source for illuminating an object. There is no electric field between the point source and the object. However, in PPM, there is a strong electric field applied between the electron source, a field emission tip and the object. The inhomogeneous electric fields around the nano-objects due to the induced charge on the object can seriously distort the wavefront of the illuminating beam when the tip–object separation is very small. Such a PPM is used in this work and it is our objective to clarify the effect of those non-uniform fields near the sample.

In this work, we have used a home-made PPM with a highly coherent single-atom electron source to image a suspended and isolated single-walled carbon nanotube (SWNT), which consists of a rolled-up graphene sheet and is one of the thinnest 1D nano-objects that can be prepared easily. The thickness of an SWNT is equivalent to two graphene layers and thus the low-energy electron beam may pass through it with only small absorption. This would provide us a unique opportunity to test whether or not the interference patterns recorded in PPM images are the electron holograms proposed by Gabor, i.e. whether they are mainly caused by the interference between the reference wave and the phase-shifted wave after penetrating the SWNT. Here, the isolated SWNT is confirmed by transmission electron microscope (TEM) imaging. By fitting the interference patterns in PPM images recorded at different magnifications with our theoretical simulations, the relative contributions of the holographic effect and the biprism effect can be determined.

2. Experimental and theoretical details

2.1. Experimental

Our experiments are carried out with a custom-made PPM. Figure 1(a) shows a schematic diagram of the setup, which is housed in an ultra-high vacuum chamber made with mu-metal. The tip used in our experiments is an Ir-covered W(111) single-atom tip (SAT) and the procedures for preparing an Ir-electroplating W(111) tip and for heat treatment in vacuum have been described earlier [23]. The tip holder is attached to a piezo-scanner that allows fine positioning of the tip and the whole assembly is mounted on a stick-slip-type linear motor, as in scanning tunneling microscopy, to allow approaching of the tip to the sample [16, 24]. The tip–sample separation, z_1, and magnification of the PPM, $\boldsymbol{M} = (z_1 + z_2)/z_1$, can thus be changed. During our experiments, the sample holder is grounded and the tip is negatively biased to a voltage V to extract electrons from the tip end. The projected pattern is recorded with a micro-channel plate (MCP; Hamamatsu F2226-24PGFX, 77 mm in diameter) and a phosphor screen, which are ∼170 mm behind the sample. A CCD camera (Alta U2000, 1600 × 1200 pixels, 16 bit dynamic range) is placed behind the screen to take images. During electron emission, the Ir-covered W(111) SAT is kept at room temperature. Our sample holder is a microfabricated Si_3N_4 membrane-coated with an Au film of 50 nm thickness. The inset in the middle of figure 1(a) is an SEM image of a part of the membrane, which contains periodic holes with a width of 4.2 μm and allows suspension of SWNTs across the holes. In our experiments, the distance z_1 typically starts from a few millimeters and gradually decreases to achieve a higher magnification in PPM images. In this work, we have obtained the interference patterns of a suspended SWNT at several different values of z_1. By comparing the interference patterns with theoretical simulations (described later), we try to determine the different contributions to the contrast in PPM images.

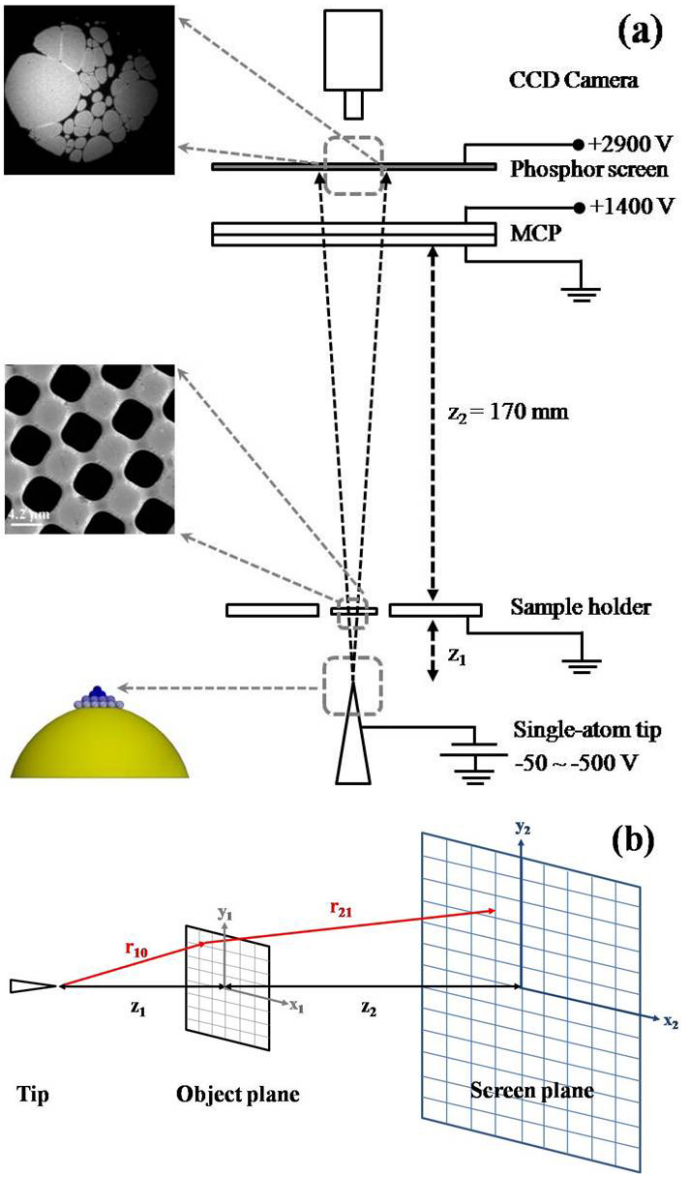

Figure 1. (a) Schematic diagram of the low-energy electron PPM. The magnification of the sample at the screen is $(z_1 + z_2)/z_1$, where z_2 is 170 mm and z_1 is the tip-sample separation. The electron beam is extracted from the topmost atom of the pyramidal single-atom tip (at the lower left-hand side). At the middle left-hand side is an SEM image of a part of a thin micro-structured Si_3N_4 membrane sample support with a periodic rectangular hole pattern (periodicity $10\,\mu m \times 10\,\mu m$). The corresponding PPM image is shown at upper left-hand corner, which is taken at room temperature and the tip bias is -460 V. (b) The relative coordinates between the electron point source, the object plane and the screen plane.

After imaging with the PPM, the sample is transferred to a TEM for high-resolution imaging. We can locate the same area after transferring the sample to TEM through identification of the same markers, some defect patterns on the microfabricated membrane.

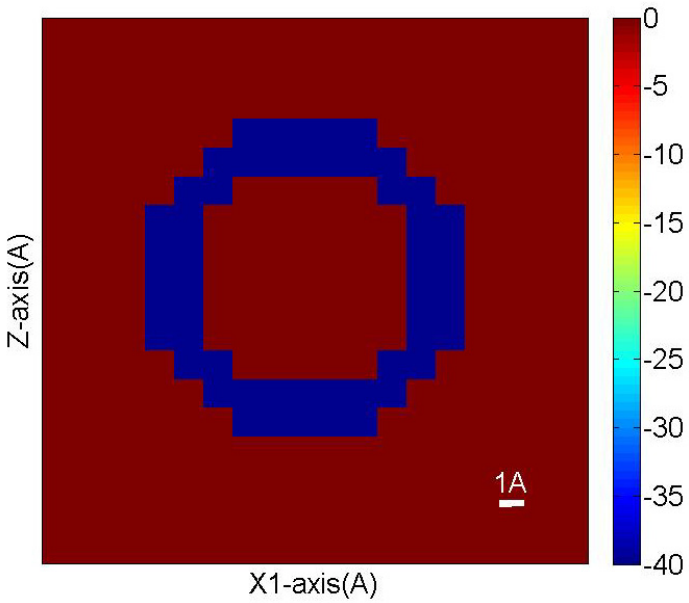

Figure 2. Cross-section of the potential distribution of our SWNT model. The scale bar shows the unit of this discrete model. The potential inside the wall or the shell of the cylinder is determined to be −40 eV after fitting experimental data. The rest part is the empty space with a potential of 0 eV.

The defect patterns can be seen easily on low-magnification images of the sample in both PPM and TEM. The relative position between the markers and the area we intend to image at high magnifications are recorded. High-resolution TEM images allow us to identify whether the objects are individual SWNTs or SWNT bundles and to determine the magnification of PPM images, which is usually difficult when the magnification is high.

2.2. Theoretical

To understand the phase shift caused by the SWNT, we have used a simple model to simulate the inner potential of the nanotube. We model the SWNT as a hollow cylinder with a length $L = 350$ nm, an *inner* diameter of 0.8 nm and an *outer* diameter of 1.1 nm. Figure 2 shows the cross-section of this model with 1 Å as the discrete unit. The potential φ is set to be a constant, φ_o, inside the wall or the shell of the cylinder and is 0 eV elsewhere.

Based on the Huygens–Fresnel principle, the electron wave function at the screen plane, $U(x_2, y_2)$, can be described as follows:

$$U(x_2, y_2) = \frac{1}{i\lambda} \iint T(x_1, y_1) \frac{\exp(ikr_{10} + ikr_{21})}{r_{10}\, r_{21}} dx_1\, dy_1, \tag{1}$$

where the electron wavelength, λ, can be calculated using the relation $\lambda = \frac{12.3}{\sqrt{V}}$A, where V is the voltage applied on the tip. The coordinates (x_1, y_1) and (x_2, y_2) define positions at the object plane and the screen plane, respectively. The coordinates used in our simulations are schematically depicted in figure 1(b). Here, we assume a spherical electron beam emitted from a SAT. It propagates a distance r_{10} to a point (x_1, y_1) on the sample plane and then propagates another distance r_{21} to a point (x_2, y_2) on the screen plane after passing through a sample.

Because r_{10} and r_{21} are much larger than the diameter of the SWNT, we can approximately treat the sample as a two-dimensional object. We introduce a transmission function $T(x_1, y_1)$ to describe the modification of the electron wave by the sample. It contains two parts: holographic (T_n) and biprism (T_v) parts. For the biprism part, it can be expected that a density of electric charge is induced on the isolated SWNT in response to a voltage applied between the tip and the SWNT. The induced charge will deform the electric potentials around the SWNT, as simulated by Weierstall *et al* [9] and by Prigent and Morin [10], and thus the SWNT may work as a convergent electron biprism.

The transmission function $T(x_1, y_1)$ can then be written as follows:

$$T(x_1, y_1) = T_n(x_1, y_1) \times T_v(x_1, y_1),$$

where $T_n(x_1, y_1)$ accounts for the absorption and phase shift when an electron beam passes through the sample (the holographic part) and $T_v(x_1, y_1)$ accounts for the distortion of the wavefront caused by the electric potential around the SWNT (the biprism part). $T_n(x_1, y_1)$ can be written as

$$T_n(x_1, y_1) = \exp\left[-\mu(x_1, y_1) + i\psi(x_1, y_1)\right], \tag{2}$$

where the amplitude part is included in $\mu(x_1, y_1) = \int m(x_1, y_1, z)\,dz$ with $m(x_1, y_1, z)$ describing the absorption in the sample and the phase shift is included in $\psi(x_1, y_1) = \frac{2\pi}{\lambda}\int [n(x_1, y_1, z) - 1]\,dz$ with $n(x_1, y_1, z)$ being the refraction index of the sample. It has been a known fact in the community of electron holography that the refraction index varies with the electron energy E through a relationship [25]

$$n = \sqrt{1 + \frac{\varphi(x_1, y_1, z)}{E}} \approx 1 + \frac{\varphi(x_1, y_1, z)}{2E},$$

and hence

$$\psi(x_1, y_1) = \frac{\pi}{\lambda E}\int \varphi(x_1, y_1, z)\,dz, \tag{3}$$

where $\varphi(x_1, y_1, z)$ is a local potential at (x_1, y_1, z), which is set to be φ_o inside the wall or the shell of the cylinder and is 0 eV elsewhere.

To consider the distortion of the wavefront caused by the induced charge on the sample (the biprism effect), we can define

$$T_v(x, y) = \exp\left[\frac{i\pi}{\lambda E}\int eV(x, y, z)\,dz\right]. \tag{4}$$

Since our sample is an isolated SWNT, we can model the induced charge in the sample as a line charge with a uniform charge density ρ. An electric potential distribution

$$V(\vec{r}, z) = \frac{1}{4\pi\varepsilon}\int \frac{\rho}{\left|\vec{r} - \vec{r}'\right|}\,d^3r'$$

around this line charge can be created in our simulation [10] and the distortion of the wavefront can thus be calculated from equation (4).

Since z_2 is much larger than x_1, y_1 and z_1 when $M > 10^4$, we can expand r_{21} with Taylor series to the second order:

$$r_{12} = \sqrt{(x_1 - x_2)^2 + (y_1 - y_2)^2 + (z_1 - z_2)^2} \approx z_2\left(1 + \frac{1}{2}\frac{(x_1 - x_2)^2 + (y_1 - y_2)^2}{z_2^2}\right).$$

In equation (1), it was assumed that a point source emits spherical waves with a uniform intensity. Here we need to modify it into a beam with a narrow Gaussian profile as measured from a realistic single-atom electron source [16, 24]

$$\frac{\exp(\mathrm{i}kr_{10})}{r_{10}} \rightarrow \exp\left(\frac{x_1^2+y_1^2}{\sigma z_1^2}\right) \times \frac{\exp(\mathrm{i}kr_{10})}{r_{10}},$$

where $\sigma = 0.005$. After rearranging equation (1), we obtain

$$U(x_2, y_2) = \frac{A \cdot \exp(\mathrm{i}kz_2) \exp\left[\frac{\mathrm{i}k}{2z_2}\left(x_2^2+y_2^2\right)\right]}{\mathrm{i}z_2\lambda} \times \iint T(x_1, y_1) \times g(x_1, y_1) \times \exp\left[\frac{-\mathrm{i}k}{z_2}(x_2x_1 + y_2y_1)\right] \mathrm{d}x_1\, \mathrm{d}y_1,$$

where

$$g(x_1, y_1) = \exp\left(\frac{x_1^2+y_1^2}{\sigma z_1^2}\right) \times \frac{\exp(\mathrm{i}kr_{10})}{r_{10}} \exp\left[\frac{\mathrm{i}k}{2z_2}\left(x_1^2+y_1^2\right)\right].$$

It has the mathematical form of the Fourier transform and, hence, we can calculate it with a fast Fourier transform algorithm:

$$U(x_2, y_2) = \frac{A \cdot \exp(\mathrm{i}kz_2) \exp\left[\frac{\mathrm{i}k}{2z_2}\left(x_2^2+y_2^2\right)\right]}{\mathrm{i}z_2\lambda} \times FT\{T(x_1, y_1) \times g(x_1, y_1)\}. \tag{5}$$

Since only the electron intensity is measured experimentally, it can be calculated as follows:

$$I(x_2, y_2) = |U(x_2, y_2)|^2 = \left|\frac{1}{\lambda z_2} FT\{g(x_1, y_1) \times T_{\mathrm{n}}(x_1, y_1) \times T_{\mathrm{v}}(x_1, y_1)\}\right|^2. \tag{6}$$

To verify the potential we used for the SWNT in figure 2, we have also carried out *ab initio* first principle calculation to obtain the potential inside a (15,0) SWNT, which has an outer diameter of 1.1 nm. The phase shift for the electron wave just passing through the SWNT is calculated and compared with the phase shift computed from our cylindrical model. In the *ab initio* calculation, we obtain the potential $\varphi(x_1, y_1, z)$ of the SWNT. The electronic structures are calculated using the full-potential projected augmented wave method [26, 27] as implemented in the VASP package [28–30] within the local-density approximation. The SWNTs are simulated by an infinitely long (15,0) tube surrounded by at least 10 Å of vacuum space. The geometry of the tube has been optimized with the residue atomic forces less than 0.01 eV Å^{-1}. Self-consistent electronic structure calculations are performed over 90 k-points in the 1D Brillouin zone using 381 024 plane waves with a cutoff energy of 400 eV. We can then calculate the phase shift $\psi(x, y)$ of the electron wave right after passing through the SWNT by using equation (3) and by assuming that the path of electron is almost a straight line because the SWNT is very thin. Multiple scattering is also ignored. The phase shift calculated by using the inner potential obtained by *ab initio* calculation is shown in figure 3(a). The phase shift calculated by using our cylindrical model with a constant potential $\varphi_{\mathrm{o}} = -40$ eV is shown in figure 3(b). We can compare these two results shown in figures 3(a) and (b) by averaging the phase shift shown in figure 3(a) along the y-axis or the cylindrical axis. Figure 3(c) shows the

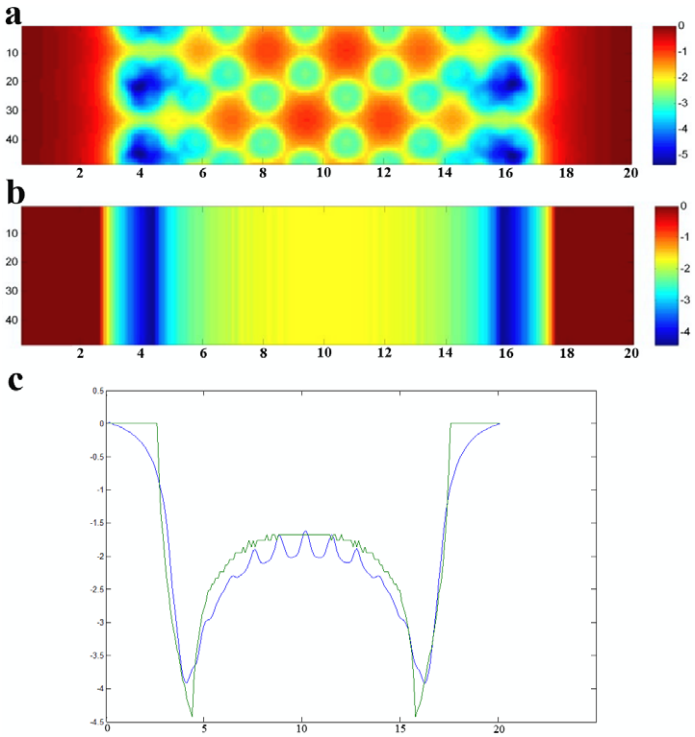

Figure 3. Phase shift function $\psi(x, y)$ of the electron beam after passing an SWNT of diameter 1.1 nm. (a) Results obtained by *ab initio* calculations on a (15,0) SWNT. (b) Results obtained based on our cylinder model with a constant wall potential of -40 eV. The pixel size is 0.084 Å $\times$ 0.084 Å. (c) Phase shift profile averaging along the y-axis or the cylindrical axis. The green line is the profile along the x-axis obtained from our cylinder model and the blue line from *ab inito* calculations.

profile of phase shift along the x-axis. The beam direction is along the z-axis. The green line obtained from the cylindrical model agrees quite well with the blue line obtained from the *ab initio* results.

3. Results and discussion

Figures 4(a)–(f) show PPM images taken with gradually increasing magnification by moving an Ir-covered W(111) SAT closer to the sample. Figure 4(a) is a projection image of an individual SWNT suspended by other thicker SWNT structures, which is confirmed by TEM image shown in figures 4(g) and (h). The dark regions in the PPM image result from the thick SWNT structure regions, which is opaque for the low-energy electron beam. Near the middle of the PPM image in figure 4(a), we can see an interference pattern of low contrast at the position of the suspended SWNT. Note that the central fringe is wider and darker than the outer fringes. With decreasing z_1, the tip extraction voltage decreases and the number of observable fringes increases (figures 4(b)–(f)). In figures 4(a)–(d), the center fringe becomes brighter as the tip approaches and is wider than the outer fringes. However, in figures 4(e) and (f), three or more fringes in the center of the interference pattern exhibit the same width. The regular spacing of

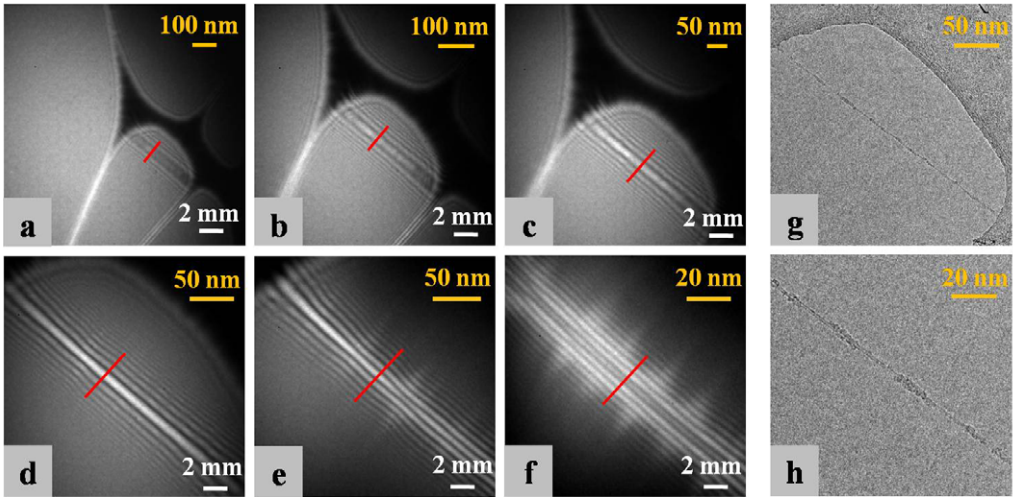

Figure 4. Projection images of a suspended SWNT taken at different magnifications. The tip and the sample are maintained at room temperature during imaging. (a) $z_1 = 11\,\mu$m, $V = -340$ V; (b) $z_1 = 6.7\,\mu$m, $V = -300$ V; (c) $z_1 = 5\,\mu$m, $V = -280$ V; (d) $z_1 = 3.2\,\mu$m, $V = -240$ V; (e) $z_1 = 2.4\,\mu$m, $V = -220$ V; and (f) $z_1 = 1.8\,\mu$m, $V = -210$ V. The white scale bars at the lower right corner in each image indicate a length of 2 mm on the screen; the yellow scale bars at the upper right corner indicate a length on the sample plane. Panel (g) is a TEM image of the suspended SWNT and the surrounding structure. Panel (h) is a higher resolution TEM image of the SWNT. Note that there are a few amorphous carbon clusters on the SWNT, which may contribute to the non-uniform fringe intensity along the tube in the PPM images.

central fringes is a clear indication of the normal action of the nanoprism [14]. In figure 4(f), interestingly, the central fringe becomes slightly darker than the other fringes again.

We have tried to simulate the intensity line profiles across the fringe patterns (indicated by red lines) of the suspended SWNT shown in figure 4. Two parameters, including the inner potential φ_o and the linear charge density, are tuned to obtain the best fit of the interference patterns obtained with our PPM at several different magnifications.

Figure 5 shows the measured profiles (red lines) and the best-fit simulated profiles (blue lines). It can be seen that both the fringe spacing and the intensity distribution fit well in all these profiles. Our extensive simulations indicate that there is a negligibly small induced charge when z_1 is larger than $\sim 10\,\mu$m, and the interference pattern mainly comes from the holographic contribution. However, the biprism effect becomes more important with deceasing z_1. When z_1 is smaller than $5\,\mu$m, the biprism effect, T_V, dominates over the holographic effect, T_n, in the simulated profiles. The biprism effect alone can provide good fit to the line profiles in figures 5(c)–(f), and T_n has very little contribution in these profiles. From fitting the line profiles in figure 5(a), we find that the holographic effect, T_n, is responsible for the fringe pattern and the cylinder potential is determined to be about -40 eV. Here we choose $m = 0.003$ ($\sim$10% total absorption) for convenient fitting to account for the good transparency of the SWNT. For the profiles in figures 5(b)–(e), the biprism effect has to be included in order to obtain a bright central fringe. The obtained charge density ρ increases from $0.0035\,\mathrm{e\,nm^{-1}}$ in figure 5(b) to

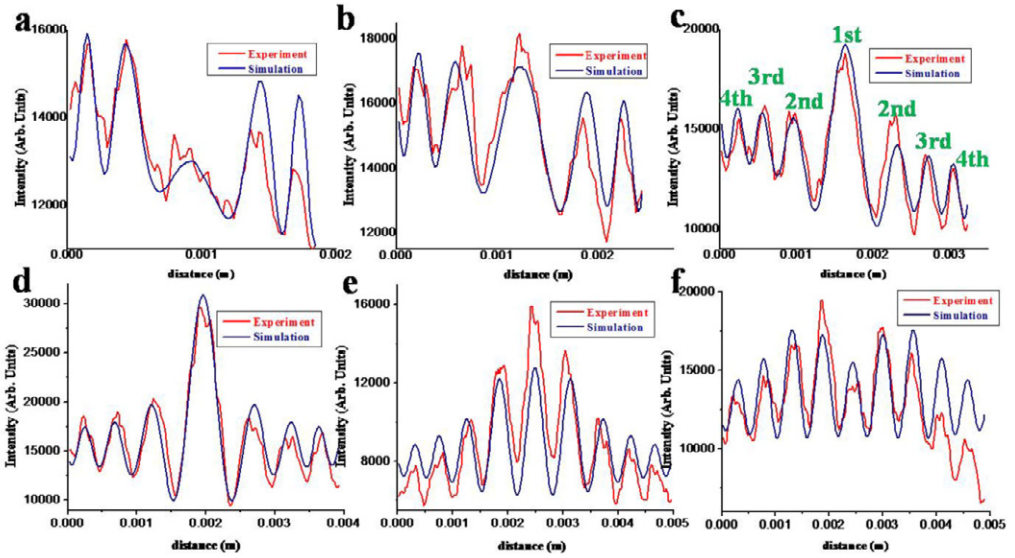

Figure 5. Line profiles of the experimental (red line) and simulated (blue line) results along the red lines in figure 4. (a) $z_1 = 11\,\mu$m, (b) $z_1 = 6.7\,\mu$m, (c) $z_1 = 5\,\mu$m, (d) $z_1 = 3.2\,\mu$m, (e) $z_1 = 2.4\,\mu$m and (f) $z_1 = 1.8\,\mu$m.

$0.08\,\mathrm{e\,nm^{-1}}$ in figure 5(f). Interestingly, the change in the interference patterns of the SWNT shown in figures 4(c)–(f) resembles different actions of the electron biprism experiment [31].

Figure 6 shows the simulated images of an SWNT in the best-fit conditions. These exhibit very similar characteristics to those seen in PPM images of the suspended SWNT in figure 4. In the simulations, we also adjust the center of the Gaussian beam profile relative to the position of the suspended SWNT. This can provide the unsymmetrical fringe intensity profile on both sides of the central fringe as observed experimentally. Table 1 shows the fitting error between the experimental profiles and the simulated results. The fringe spacing fits well with deviation less than 10%.

Binh *et al* [11] reported their observation of free-standing SWNTs with a PPM. Through numerical simulations, they determined that the bright lines without interference fringes were PPM images of individual SWNTs. They also determined the interference patterns related to different bundled tubes. The pattern they attributed to an individual SWNT is significantly different from the patterns shown here in figure 4. Some parameters in their simulations were probably incorrect. Clearly, making a comparison with TEM images aids our interpretation of PPM images greatly.

In PPM, when the tip–sample separation is larger than $10\,\mu$m, the magnification and the spatial resolution increase with decreasing tip–sample distance because there is little induced charge on the SWNT. In this regime, the interference fringes mainly come from the holographic part, i.e. the phase shift of the electron wave passing through the SWNT. Thus the interference patterns can be considered as holograms, which contain information about the internal structure of the object. However, when the tip–sample separation is smaller than $5\,\mu$m, the biprism effect becomes dominant and the interference pattern mainly comes from the electron waves from both sides of the SWNT, which contains little information about the internal structure of the object. These results clearly indicate that there is a resolution limit for PPM images of 1D objects. It

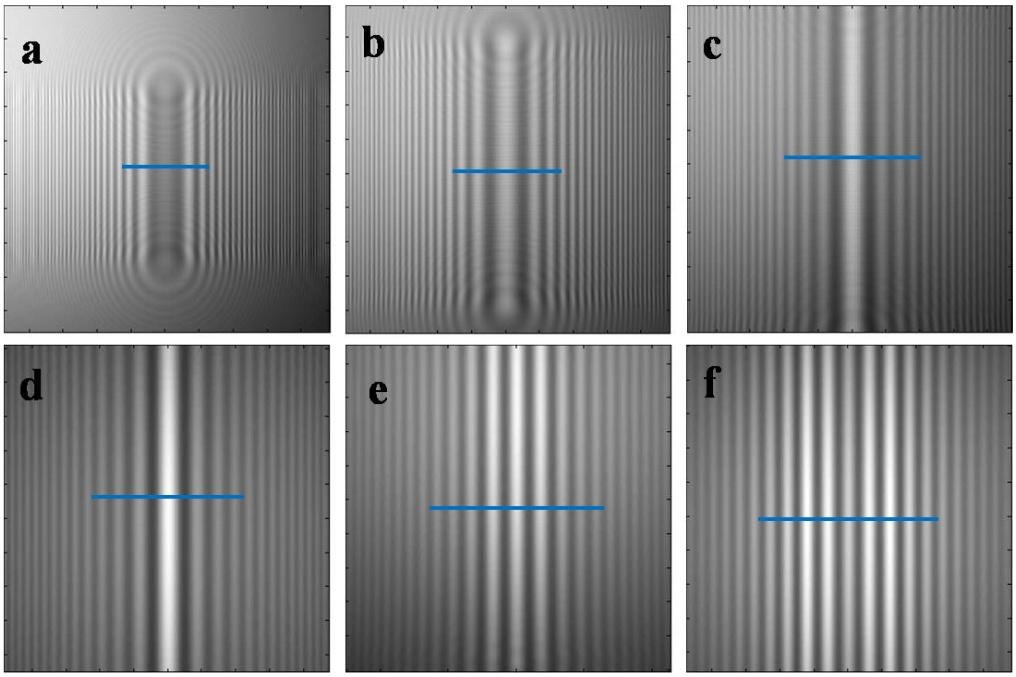

Figure 6. Simulation images of a suspended SWNT. (a) $z_1 = 11\,\mu$m, $\rho = 0\,\mathrm{e\,nm^{-1}}$; (b) $z_1 = 6.7\,\mu$m, $\rho = 0.0035\,\mathrm{e\,nm^{-1}}$; (c) $z_1 = 5\,\mu$m, $\rho = 0.0125\,\mathrm{e\,nm^{-1}}$; (d) $z_1 = 3.2\,\mu$m, $\rho = 0.028\,\mathrm{e\,nm^{-1}}$; (e) $z_1 = 2.4\,\mu$m, $\rho = 0.05\,\mathrm{e\,nm^{-1}}$; and (f) $z_1 = 1.8\,\mu$m, $\rho = 0.08\,\mathrm{e\,nm^{-1}}$.

Table 1. The fitting error between the measured fringe spacing and the simulated fringe spacing.

$z_1(\mu\mathrm{m})$, E (eV), $q(\mathrm{e\,nm^{-1}})$	1st	2nd	3rd	4th	5th
11, 340, $q = 0$	2.67%	5%	12.5%	NA	NA
6.7, $E = 300$, $q = 0.0035$	2.56%	4.65%	6.67%	NA	NA
5.0, $E = 280$, $q = 0.0125$	2.63%	6.3%	5.5%	6.25%	NA
3.2, $E = 240$, $q = 0.028$	2.5%	3.4%	4%	10%	NA
2.4, $E = 220$, $q = 0.05$	3%	5.1%	3.6%	9.8%	5%
1.8, $E = 210$, $q = 0.08$	1.85%	3.7%	5%	11%	6.6%

may explain why the spatial resolution of PPM achieved so far never exceeds 2 nm [6, 9, 12, 13, 15, 18]. In 1994, Shedd first doubted the atomic resolution image reconstruction in PPM [6]. A review paper also considered the electric fields around the imaged object as an obstacle to achieve a spatial resolution better than 2 nm [18]. Now some *research groups* are taking PPM images of two-dimensional objects, such as few-layer graphene [32–34]; it would be interesting to investigate whether atomic resolution can be achieved.

It is attractive to image biological or organic molecules with low-energy electrons due to the low radiation damage and high scattering cross sections. In particular, it has become routine to prepare metal tips ending with only one atom or a few atoms, which can field emit highly coherent electron beams. However, electrons of 20–500 eV may not be suitable for such

a purpose because their inelastic mean free paths (below 1 nm) are smaller than the thickness or diameter of most biological molecules. For coherent electron imaging of biological molecules, there is a need to go to a higher energy range, e.g. above 1 keV, to reach a mean free path larger than the thickness of the objects. In addition, the high spatial frequency components of the elastically scattered object wave travel in large angles relative to the propagation direction of the primary beam. To reconstruct the high spatial frequency components of the object from the interference patterns (or holograms), it is essential that the primary beam also has a large diverging angle. Currently, a coherent electron beam field emitted from a sharp tip of a few atoms typically has a very small opening angle (half angle of 3° or smaller); thus there is a need to make use of a lens to focus the narrow electron beam into a small point with a large diverging beam, as originally proposed by Gabor. An alternative is to perform coherent diffractive imaging with the narrow beam. If high-angle diffraction patterns can be obtained, a high-resolution imaging of thin objects, such as protein molecules, might be achieved.

4. Conclusions

The main purpose of this work is to clarify the relative contributions from the holographic effect and the biprism effect in the formation of the interference patterns of an isolated SWNT in PPM images. Through a comparison of experimental imaging and theoretical fitting, we have found that the interference patterns seen in PPM images can be viewed as electron holograms when the magnification is smaller than $\sim 1.7 \times 10^4$, because there is little induced charge on the SWNT. The biprism effect becomes dominant when the magnification is higher than $\sim 3.5 \times 10^4$, and the interference pattern can no longer be viewed as a hologram. Now the isolated SWNT works as the smallest biprism for the low-energy electron beams. Due to the weak holographic contribution, it might be very difficult to reconstruct the atomic structure of the SWNT from the high-magnification interference patterns. The results may improve the understanding of coherent electron imaging of nano-materials.

Acknowledgment

This work was supported by National Science Council (grant NSC95-2112-M-001-009) and Academia Sinica (grant AS-99-TP-A02), Republic of China.

References

[1] Stocker W, Fink H W and Morin R 1989 *Ultramicroscopy* **31** 379
[2] Fink H W, Stocker W and Schmid H 1990 *Phys. Rev. Lett.* **65** 1204
[3] Kreuzer H J, Nakamura K, Wierzbicki A, Fink H W and Schmid H 1992 *Ultramicroscopy* **45** 381
[4] Spence J C H, Qian W and Melmed A J 1993 *Ultramicroscopy* **52** 473
[5] Binh V T, Semet V and Garcia N 1994 *Appl. Phys. Lett.* **65** 2493
[6] Shedd G M 1994 *J. Vac. Sci. Technol.* A **12** 2595
[7] Gölzhäuser A, Völkel B, Jäger B, Zharnikov M, Kreuzer H J and Grunze M 1998 *J. Vac. Sci. Technol.* A **16** 3025
[8] Park J Y, Kim S H, Suh Y D, Park W G and Kuk Y 1999 *Rev. Sci. Instrum.* **70** 4304
[9] Weierstall U, Spence J C H, Stevens M and Downing K H 1999 *Micron* **30** 335
[10] Prigent M and Morin P 2000 *J. Microsc.* **199** 197

[11] Binh V T, Vincent P, Feschet F and Bonard J M 2000 *J. Appl. Phys.* **88** 3385
[12] Georges V, Bardon J, Degiovanni A and Morin R 2001 *Ultramicroscopy* **90** 33
[13] Gölzhäuser A, Völkel B, Grunze M and Kreuzer H J 2002 *Micron* **33** 241
[14] Cho B, Ichimura T, Shimizu R and Oshima C 2004 *Phys. Rev. Lett.* **92** 246103
[15] Eisele A, Völkel B, Grunze M and Gölzhäuser A 2008 *Z. Phys. Chem.* **222** 779
[16] Chang C C, Kuo H S, Hwang I S and Tsong T T 2009 *Nanotechnology* **20** 115401
[17] Weber D H, Beyer A, Völkel B and Gölzhäuser A 2010 *Small* **12** 1264
[18] Beyer A and Gölzhäuser A 2010 *J. Phys.: Condens. Matter* **22** 343001
[19] Gabor D 1948 *Nature* **161** 777
[20] Morton G A and Ramberg E G 1939 *Phys. Rev.* **56** 705
[21] Germann M, Latychevskaia T, Escher C and Fink H W 2010 *Phys. Rev. Lett.* **104** 095501
[22] Zangwill Z A 1998 *Physics at Surfaces* (Cambridge: Cambridge University Press) p 21
[23] Kuo H S, Hwang I S, Fu T Y, Wu J Y, Chang C C and Tsong T T 2004 *Nano Lett.* **4** 2379
[24] Hwang I S, Kuo H S, Chang C C and Tsong T T 2010 *J. Electrochem. Soc.* **157** 7
[25] Tonomura A 1984 *J. Electron Microsc.* **33** 101
[26] Blochl P E 1994 *Phys. Rev.* B **50** 17953
[27] Kresse G and Joubert D 1999 *Phys. Rev.* B **59** 1758
[28] Kresse G and Hafner J 1993 *Phys. Rev.* B **48** 13115
[29] Kresse G and Furthmuller J 1996 *Comput. Mater. Sci.* **6** 15
[30] Kresse G and Furthmuller J 1996 *Phys. Rev.* B **54** 11169
[31] Lichte H and Lehmann M 2008 *Rep. Prog. Phys.* **71** 016102
[32] Mutus J Y, Livadaru L, Robinson J T, Urban R, Salomons M H, Cloutier M and Wolkow R A 2011 *New J. Phys.* **13** 063011
[33] Vieker H, Beyer A, Blank H, Weber D H, Gerthsen D and Gölzhäuser A 2011 *Z. Phys. Chem.* **225** 1433
[34] Longchamp J N, Latychevskaia T, Escher C and Fink H W 2012 *Appl. Phys. Lett.* **101** 113117